TECHNICAL PAPER

The microstructures, mechanical properties, and temperature distributions in nodular cast iron friction-welded joint

Radosław Winiczenko[1] · Mieczysław Kaczorowski[2] · Andrzej Skibicki[3]

Abstract

The paper focuses on an experimental topic relating to the field of friction welding process of a nodular cast iron. The microstructures, phase transformation, temperature distributions, microhardness, and tensile test are all studied within the framework of the paper in question. Maximum temperature measurements in the axial center and periphery of the analyzed joints were equal to 950 and 840 °C, respectively. Both temperature and increasing temperature gradient at the axial center were higher than those at the periphery. The maximum tensile strength of the examined friction-welded nodular cast iron joints was 53% of that of the parent metal. The welding region was composed of deformed graphite nodules, coarse pearlite, proeutectoid ferrite, and acicular martensite. Highly deformed graphite nodules were distributed along the weld interface due to the material flow in the thermo-mechanically affected zone (TMAZ). In the central zone, graphite displayed a striped configuration and ferrite transformed into a martensite structure. In the peripheral region, graphite surrounded by martensite kept the form of individual granules. Maximum hardness at the interface in the TMAZ and the heat-affected zone reached 603 HV and 345 HV, respectively. The executed microstructure analysis showed that the cracks started occurring mostly at the interface of the deformed graphite nodules and then spread through the grain boundaries of metal matrix. The fracture surface appearance showed a cleavage fracture in the peripheral zone and a little dimple fracture around graphite nodules in the central zone.

Keywords Friction welding · Nodular cast iron · Temperature distribution · Microstructure · Tensile test · Microhardness

✉ Radosław Winiczenko
   rwinicze@poczta.onet.pl

   Mieczysław Kaczorowski
   m.kaczorowski@wip.pw.edu.pl

   Andrzej Skibicki
   askibic@utp.edu.pl

1 Faculty of Production Engineering, Warsaw University of Life Sciences, Nowoursynowska 166, 02-787 Warsaw, Poland

2 Department of Mechanics and Weaponry Technology, Warsaw University of Technology, Narbutta 85, 02-524 Warsaw, Poland

3 Faculty of Mechanical Engineering, Bydgoszcz University of Science and Technology, Al. prof. S. Kaliskiego 7, 85-796 Bydgoszcz, Poland

1 Introduction

Nodular cast iron (also called ductile or spheroidal graphite cast iron) is much stronger and has a notably higher elongation than other grade cast irons. A relatively high strength and toughness of nodular cast iron are advantageous when it comes to numerous structural applications such as crankshafts, steering knuckles, brackets, valves, truck axles, hubs, water pipes, and many others [1].

Mechanical properties of nodular cast irons are directly associated with their metal matrix microstructure. The as-cast matrix microstructure of nodular cast irons may be completely ferritic, completely pearlitic, or be a combination of pearlite and ferrite, with a spheroidal graphite distributed in the matrix. The microstructural properties are affected by the solidification-cooling rate associated with the section size of castings, as well as that of alloying elements [2].

Many techniques and special materials are available that allow for repair welding of nodular cast iron castings, for joining nodular cast iron to itself, as well as to other ferrous materials. The aforementioned welding methods include shielded metal arc welding, flux cored arc welding, gas metal arc welding, gas tungsten arc welding, submerged arc welding, diffusion bonding, impact-electric current discharge joining, laser welding, oxyacetylene powder welding, and lately—friction stir processes [3].

When nodular cast iron castings are being repaired or joined by means of traditional fusion welding technologies, their high carbon content (more than 3.5%) may cause the formation of hard brittle phases, namely the cementite carbides and martensite in the fusion zone and heat-affected zone (HAZ). Carbon atoms of nodular cast iron diffuse into austenite during welding and form martensite and carbides at the weld interface while cooling [4]. These give rise to poor elongation properties and high hardness values, as described in another paper [5]. The structural transformations result in the reduction of ductility to a level where the susceptibility to cracking is so high that either a spontaneous post-welding cracking of the joint takes place, or cracks are generated when the first operational load is applied [6]. Therefore, welding of nodular cast iron, likewise welding other cast irons, requires special precautions to obtain optimum properties in the welded metal and the adjacent HAZ. Brittle martensite can be tempered to a lower strength, yet more ductile structure through preheating or post weld heat treatments. Some welding procedures are designed to reduce the size of the HAZ and thus minimize cracking [7].

While the main goal is to avoid the formation of excess cementite in the metal matrix, which makes the bonded region brittle, in nodular cast iron an additional objective based on retaining a spheroid form of graphite, is of almost equal importance [8]. To minimize the formation of massive carbides and high-carbon martensite, the most beneficial solution is to utilize carbon in the form of spheroids which have a low surface-to-volume ratio [9].

Friction welding is an example of welding process in which both similar and dissimilar metals can be welded by means of solid-state diffusion processes to overcome metallurgical complications associated with fusion welding. The welding method produces a weld when two or more workpieces, rotating or moving reciprocally, come into contact under pressure to produce heat and plastically displace material from the weld interface [10].

The discussed friction welding process is beneficial in terms of reducing the cost of complex forgings or castings, for example, of welding of a spindle or shaft to a cast/-forged head [11, 12]. However, in the case of friction welding of steels, numerous defects occur, including: center defects, restraint cracks, weld interface carbides, hot-shortness cracks, and porosity, which may lead to the failure of the friction welds [13].

The main problem when it comes to friction welding of nodular cast iron is free graphite precipitations which have lubricating properties that reduce the efficiency of the welding process. During the friction welding process, graphite nodules are deformed or fragmented, thus creating an unfavorable microstructure [14–16]. Consequently, all the properties relating to strength and ductility decrease as the proportion of nonnodular graphite increases. The form of nonnodular graphite is important, because thin graphite flakes with sharp edges have an adverse effect on crack initiation [13].

Another problem is the absence of interatomic bonds in the case of friction welding of nodular cast iron caused by the formation of continuous graphite between contact surfaces. Said phenomenon is also accompanied by a large decrease of the friction coefficient, which in turn decreases the amount of heat generated at the interface. Higher pressure applied while rotating the components should support heating the joint to the melting point. However, an increase in pressure is accompanied by the formation of a network of cracks in the weld zone, mainly due to the small plasticity of nodular cast iron [17].

In recent years, a lot of studies relating to continuous friction welding [18–22] and friction stir welding processes [23, 24] of nodular cast iron to nodular cast iron or ductile to other low carbon metals have been conducted by various researchers. Knowledge on friction weld processes is oriented toward structural and mechanical properties [25, 26] and metallurgical phase transformation [27, 28], or welding parameter optimization [29, 30]. Microstructure and mechanical properties of friction nodular cast iron joints hitherto are poorly described in the literature. Only other materials, such as mild steels, have been considered in a friction welding of a truck axle-related application, where spindles are welded to axle housings [31].

The main purpose of this paper is to show the effect of temperature and welding parameters on microstructures and mechanical properties observed in friction-welded joints. As such, the tensile test, Vickers hardness test, direct temperature measurement, optical and the electron microscopy techniques were taken advantage of to conduct the discussed study.

2 Experimental

The chemical composition and mechanical properties of a parent material selected for the study are shown in Table 1. Figure 1 shows the microstructure of the as-cast nodular with graphite nodules in a matrix. The specimens having the shape of bars of 20 mm in diameter and 100 mm in

Table 1 Alloying elements (wt%) and the mechanical properties of base material

Material	C	Si	Mn	P	S	Mg	Fe	TS	YS	EL	HB
NCI	3.42	2.86	0.49	0.030	0.050	0.025	Rest	441	316	22	165

NCI nodular cast iron, *TS* tensile strength (MPa), *YS* yield strength (MPa), *EL* elongation (%), *HB* hardness
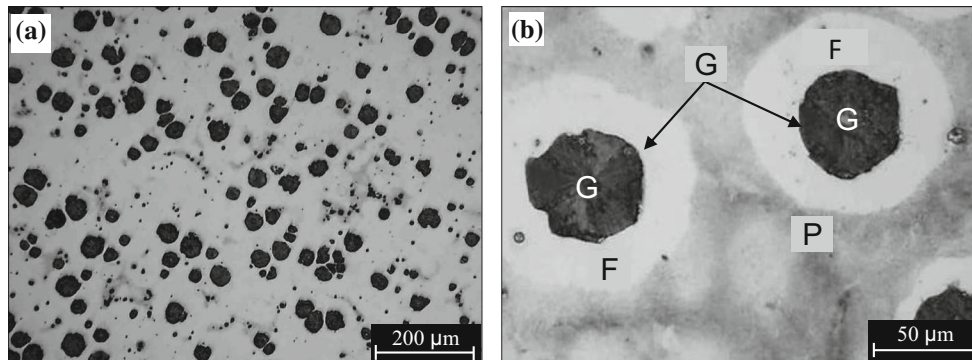
Fig. 1 Micrograph of the as-cast nodular iron Magn. ×100 **a**, **b** with ferrite surrounding graphite nodules. *G* graphite, *F* ferrite, *P* pearlite. Magn. ×500

length were cut for friction welding process. The surface for friction welding was prepared by means of using an abrasive cut-off machine. The process of joining was carried out on a continuous drive friction machine of the ZT4-13 type (ASPA, Wroclaw, Poland). Friction welding process of nodular cast iron is shown in Fig. 2. Friction welding parameters used in the experiment are shown in Table 2. During welding the primary parameters: friction pressure (FP), upsetting pressure (UP), friction time (FT), and upsetting time (UT) were continuously monitored and recorded. Few more trials have been carried out with different parameters in order to get defect free welds. The
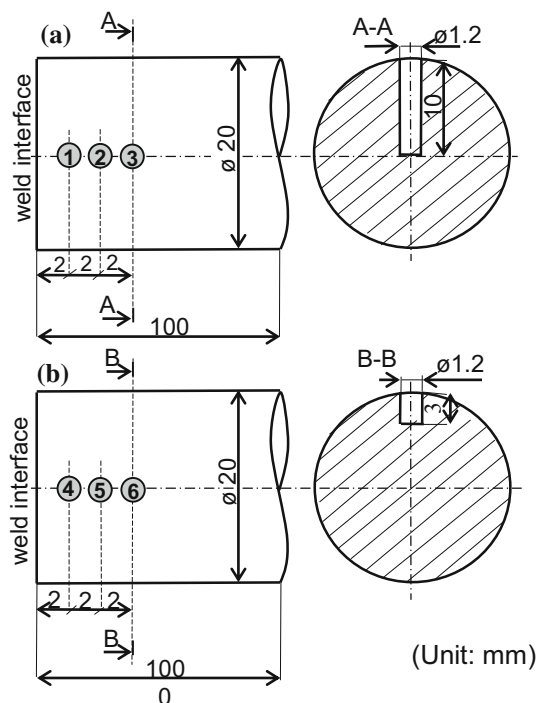

Fig. 2 Heat-affected zone formulated during of friction stage: **a** FT = 2 s, **b** FT = 17 s, **c** FT = 25 s, **d** FT = 75 s
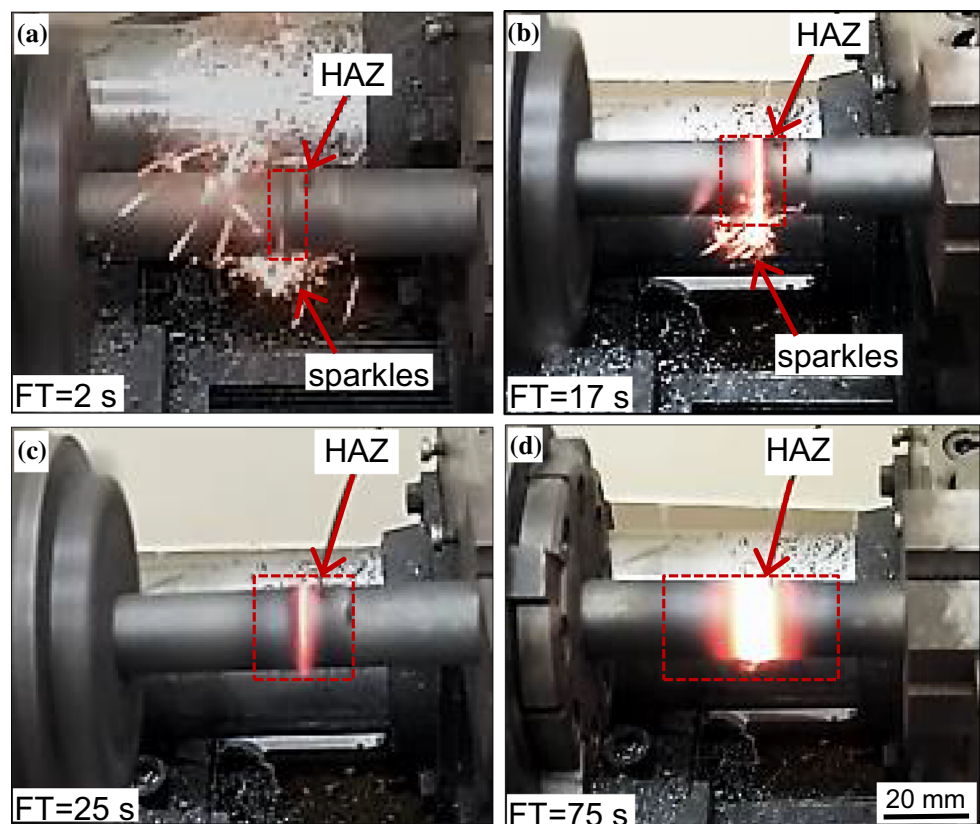
Table 2 Welding parameters and tensile strength results

Number specimen No.	Friction pressure FP (MPa)	Friction time FT (s)	Upsetting pressure UP (MPa)	Ultimate tensile strength UTS (MPa)
S1	94	30	109	84
S2	94	60	109	172
S3	94	30	143	105
S4	26	120	104	132
S5	26	90	104	103
S6	76	60	143	96
S7	76	45	143	115
S8	76	45	76	133
S9	94	150	104	187
S10	104	150	104	190
S11	118	90	104	163
S12	76	150	76	182
S13	76	180	76	188
S14	76	240	76	226

main parameters employed in this study were FP, UP, and FT. Additionally, constant rotational speed (RS = 1450 rpm) and upset time (UT = 3 s) are used in this study. The geometry of specimens used for welding process and schematic representation on the arrangement of fixing thermocouples are shown in Fig. 3. These thermocouples were installed in 1.2 mm holes at the periphery and the axial center of a joint—2, 4, and 6 mm from the interface. The thermocouples were beaded at the tip and stuck at the

measuring points with a silicate high temperature glue (TECHNICQLL, NALMAT, Trzebinia, Poland). Temperature identifiable in a close proximity to the interface of the joints was obtained with a TP202K1b2001 K-type thermocouple (NiCr–NiAl, CZAKI THERMO-PRODUCT, Raszyn, Poland) with the accuracy of ± 0.1 °C. Temperature reading was performed with a UT 325 digital thermometer (Uni-Trend Technology, Hu Men Town, China) with the requisition frequency of 1000 Hz during friction welding. Room temperature tensile tests were carried out as per ASTM:E8/E8M-11 [32] standard specimen configuration. A tensile strength test was carried out on a 100-kN servo-controlled universal testing machine (Instron). Moreover, Vicker's microhardness measurements were made across the bondline with the load of 500 g and hold time of 15 s. The microstructure of joints was examined by means of light metallography (LM), as well as a JOEL JSM-500 scanning electron microscope (SEM). The specimens were mechanically polished by means of using emery special sheets with the help of disk and bench polishing machine. The prepared specimens were etched by applying 3% Nital for inspecting the metallurgical behavior of the welded joints. The fracture surfaces of the specimens were observed in the SEM using the BEI COMPO mode, applying backscattered electrons (BSE).

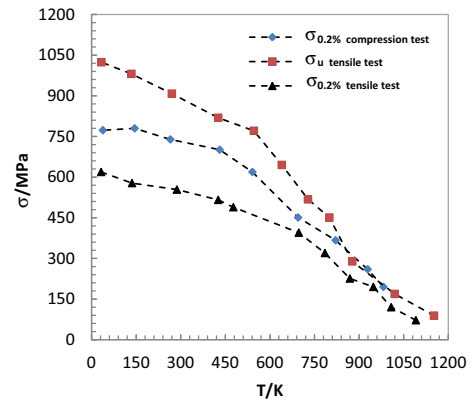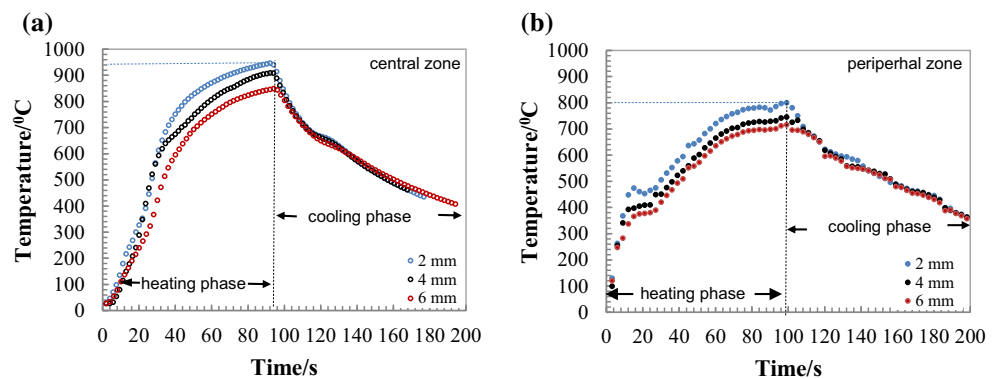## 3 Results and discussion

3.1 Process description

Figure 3 shows the heat-affected zone formulated during the friction stage of welding process. In the early phase of the welding process (Fig. 3a), the surfaces of the analyzed

Fig. 3 The schematic representation on the arrangement of thermocouples in the nonrotating sample

samples end were abraded during welding. As a result of this process, metal filings were thrown out of the joining plane. In the next phase of the welding process nodular cast iron (Fig. 3b), the graphite particles were removed from the outer surface by means of application of a high friction pressure. Oxides and other foreign materials present on the original surface were broken up and dispersed. Many sparks can be seen during the friction phase (see Fig. 3b). Moreover, during this stage, one can also observe axial displacement occurring at a slow rate, as the material at the interface starts to heat up, soften and is expelled as weld flash (Fig. 3b).

3.2 Heating phase

Time–temperature profiles at the axial center and the periphery are shown in Fig. 4a, b. Moreover, time–temperature curves were separated on the heating and cooling phases. As indicated by all of the thermocouple measurements, the analyzed metal experienced a slow rise in temperature to a peak value during welding. The peak heating temperature at $x = 2$ mm from the interface was 948 °C (see Fig. 4a) for welding time $t = 95$ s. Temperature reached peak value, but did not exceed the melting point of nodular cast iron, i.e., 1130 °C. Moreover, the increasing temperature at the axial center was about 100 °C higher than the one at the periphery specimen (see Fig. 4b). Difference in temperatures occurred due to the change of the yield strength stress of nodular cast iron with temperature (see Fig. 5). The temperature of high strength was lower than the one of low strength when the nodular cast iron base metal was deformed under the applied friction pressure. During the friction welding process, wear generated heat and consequently increased the temperature at the weld interface. Temperature increase resulted in the decrease of yield stress, which in turn allowed for an intensive plastic deformation of the welded metal at the interface. Additionally, reaction products, the microhardness distribution of the joints, and fracture morphology are all going to be discussed in the next sections.

Fig. 5 Temperature-dependent yield strength of nodular cast iron

3.3 Cooling phase

After the friction stage, the forging stage began and the metal cooled down gradually. During the cooling phase, heat was conducted away from the weld interface and lost to the surroundings through the ends of weld specimens. At 101 s, temperature started gradually dropping to 650 °C after 120 s, while at the location of $x = 6$ mm from the interface, the peak heating temperature was 850 °C. It can be seen from Fig. 4a that all three curves show a very similar cooling behavior below approximately 800 °C. The temperature curves of the weld center and peripheral zone during cooling phase (Fig. 4a, b) clearly show that temperature of the centerline is higher than that of the peripheral zone at beginning of cooling phase. The cooling curve appears to be broader than heating curve, since rate of cooling is relatively slow. The similar curve profile received in the paper [33]. The heating and cooling rates of the welding process are approximately calculated around 14 and 5 °C at the interface, respectively.

Fig. 4 Time–temperature profiles at the axial center **a**, **b** the periphery of the joint

3.4 Mathematical modeling

The empirical models used to describe the temperature curves of welding process during heating and cooling phase are shown in Tables 3 and 4. The empirical model was formulated by the authors of this study for:

a. Heating phase

$$T = \frac{a}{b + \exp(ct)} \tag{1}$$

b. Cooling phase

$$T = a - bt^c \tag{2}$$

where a, b, and c are the constants of the models; t is the welding time, s; T is calculated temperature, °C. The goodness of fit of tested mathematical models to the experimental data was evaluated with the coefficient of determination R^2. The higher R^2 the better is the goodness of fit the models. A nonlinear regression analysis was conducted to fit the models by genetic algorithm (GA) using computer program MATLAB 7.0 software (Math-Works Inc., Natick, MA).

Genetic algorithms (GA) are a search optimization technique based on natural selection and heredity mechanism. The GA has been applied in many complex optimization and search problems, outperforming traditional optimization and search methods. The basic genetic algorithm contains the following steps: (1) selection of the initial population chromosome, (2) fitness function calculation, (3) checking stopping criterion, (4) selection of chromosomes, (5) application of the genetic operators, (6) creating a new population, (7) return to step 2, and (8) the best chromosome presentation.

The fitness functions formulated in Eqs. (1) and (2) are then used to measure the fitness value for each chromosome in the GA procedure. The critical parameters in GAs are the population size, number of generations, crossover probability, and mutation rate. In this study, a population size of 60, crossover probability of 0.8, mutation rate of 0.2, and the number of iteration of 500 were employed.

3.5 Surface appearance

Figure 6a shows the appearance of the as-welded joints with different welding parameters (see Table 2). There were noticeable differences in the width of the heat-affected zones and the amount of flash produced in the welds by opting for different welding conditions. As expected, the weld made using the long time welding condition had the most flash and widest HAZ, especially while compared to welds made using other welding conditions. Symmetrical weld flashes formed on both sides of the joints can be seen. Moreover, the size of the weld flashes was dependent on friction welding parameters. Figure 6 shows that for flashes S3, S6, and S7, specimens underwent a greater deformation resulting from a high axial pressure while compared to S1, S4, and S8 flash specimens welded with less axial pressure. Furthermore, it is evident that flash scale for 60 s (see S2 specimen) was much greater than the one for 30 s (see S1 specimen) which was consistent with the longer burn-off length (upset metal). The accumulated friction heat during the welding process was sufficient to soften the base metal. When the base metal reached the plastic state, upset metal formed due to the squeezing action with friction and upsetting pressures. Additionally, burn-off length increased rapidly with the increase of friction time. Similar phenomenon has already been observed by other authors [27, 28].

A nodular cast iron friction-welded macrograph of the specimen 6 is shown in Fig. 6b. Zones with different microstructures, such as weld interface, TMAZ and HAZ as the consequence of applying the friction welding process parameters to nodular cast iron. The microstructure variations of different zones of nodular cast iron joints are discussed in Sect. 3.7.

3.6 Fracture surfaces

Figure 7 shows the macroscopic fractography of tensile specimens for varied welding parameters. All the specimens failed at the bondline during the executed tensile test without obvious plastic deformation. Thus, fracture

Table 3 Mathematical models for temperature curves during heating phase of welding process

Thermocouple position No.	Distance from weld interface x (mm)	Mathematical model $T = \frac{a}{b+\exp(ct)}$	R-squared R^2
1	2	$T = \frac{66.42}{0.074 + \exp(-0.104\,t)}$	0.9958
2	4	$T = \frac{59.50}{0.067 + \exp(-0.097\,t)}$	0.9892
3	6	$T = \frac{55.10}{0.066 + \exp(-0.0899\,t)}$	0.9961
4	2	$T = \frac{332.38}{0.404 + \exp(0.047\,t)}$	0.9492
5	4	$T = \frac{318.79}{0.414 + \exp(0.044\,t)}$	0.9568
6	6	$T = \frac{277.98}{0.3745 + \exp(0.0448\,t)}$	0.9761

Table 4 Mathematical models for temperature curves during cooling of the friction-welded joints

Thermocouple position No.	Distance from weld interface x (mm)	Mathematical model $T = a + bt^c$	R-squared R^2
1	2	$T = -148.4 + 6.907t^{-0.9238}$	0.9858
2	4	$T = -320.2 + 3.310t^{-0.732}$	0.9868
3	6	$T = -70.78 + 4.968t^{-0.8798}$	0.9954
4	2	$T = -108.6 + 4.969t^{-0.8741}$	0.9927
5	4	$T = -1655 + 7765t^{-0.2547}$	0.9792
6	6	$T = -1343 + 8247t^{-0.2992}$	0.9796

Fig. 6 Appearances of joints for different friction welding parameters **a**, **b** a typical friction-welded macrograph

3.7 Microstructure observation
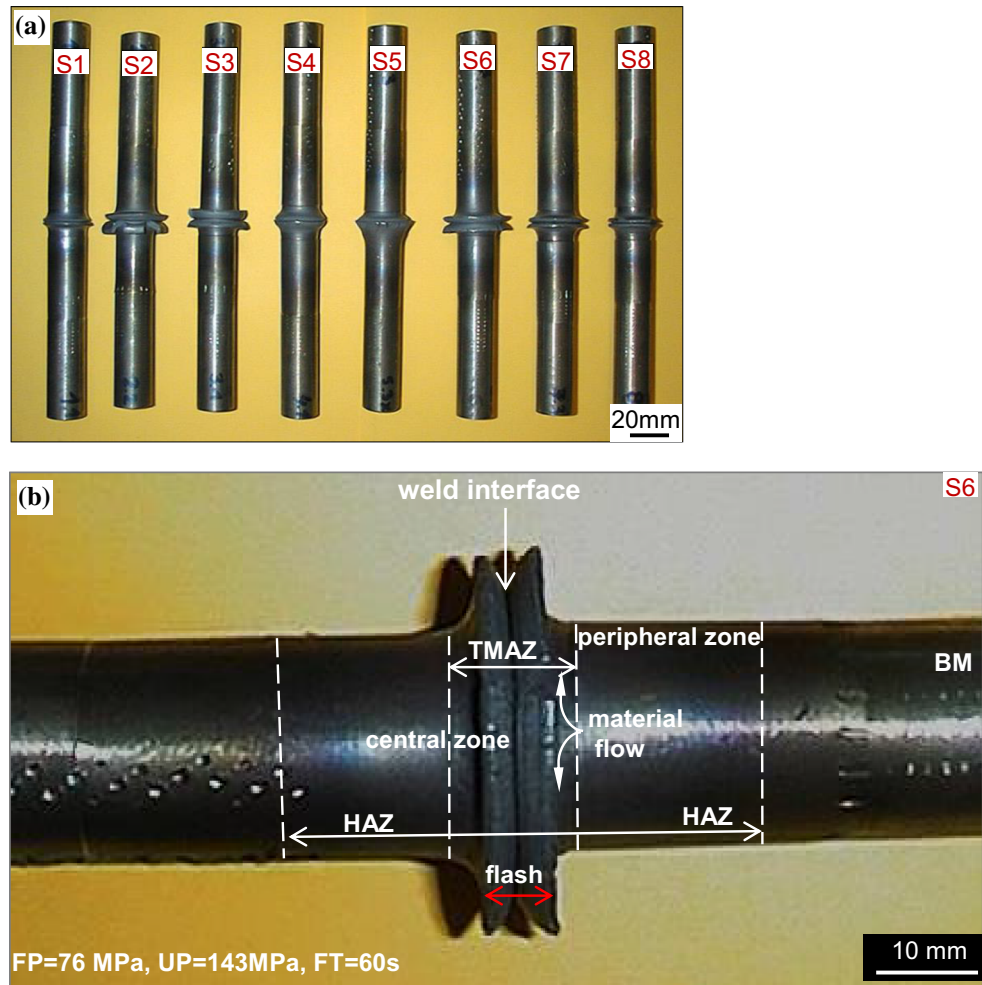
surfaces were relatively smooth and consisted of some continuous and shining regions near the periphery of the specimen. The phenomenon of incomplete bonding was detected at the center of the joint, as shown in specimens S4, S7, S10, and S11. These fractures were characterized by spiral lines of deformation distinctly, lighter plastic deformation, and insufficient heat generated in the central zone. Moreover, with increasing pressures, the fracture surface was more and more smooth as in specimens S3, S6, and S7 and relatively rough in the case of low pressure, as it can be observed in specimens S4 and S5 (Fig. 7).

Figure 8 shows a Fe–C binary diagram with major transformation boundaries, as well as the associated phases and microstructures. The carbon equivalent of nodular cast iron was used in the experiment according recommendations of the Ductile Iron Society (www.ductile.iron.org) using ANSI AWS D11. 2-89 standard equals 4.21%. The carbon equivalent of nodular cast iron is shown as the red line in Fig. 8.
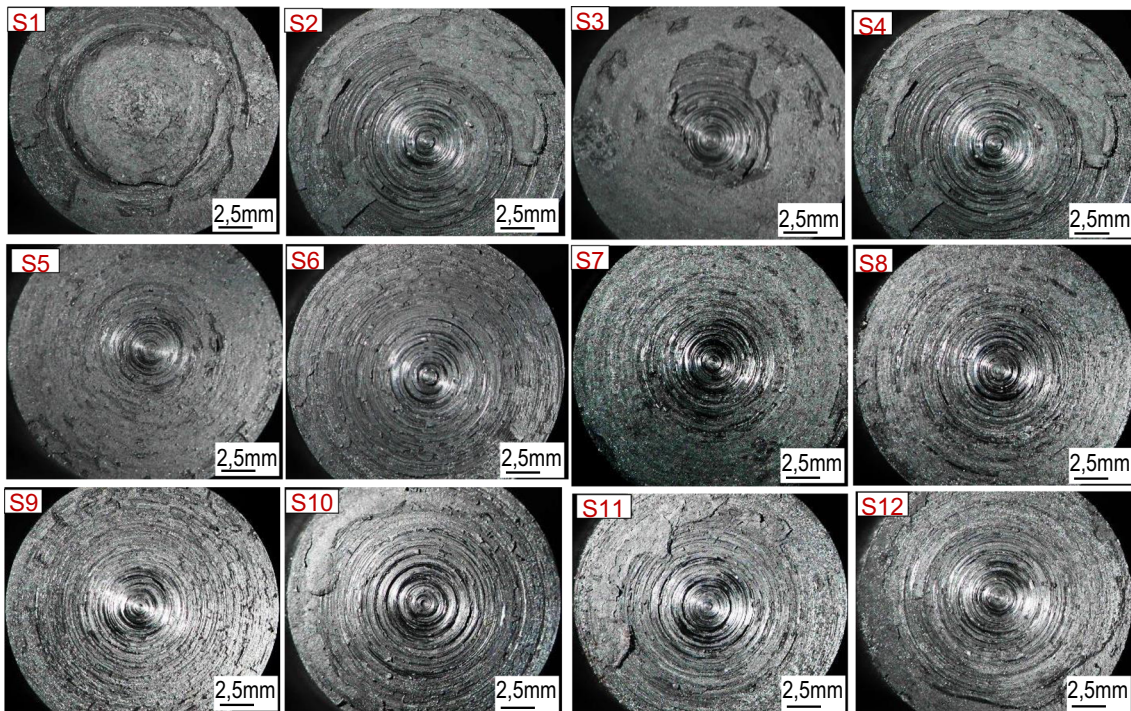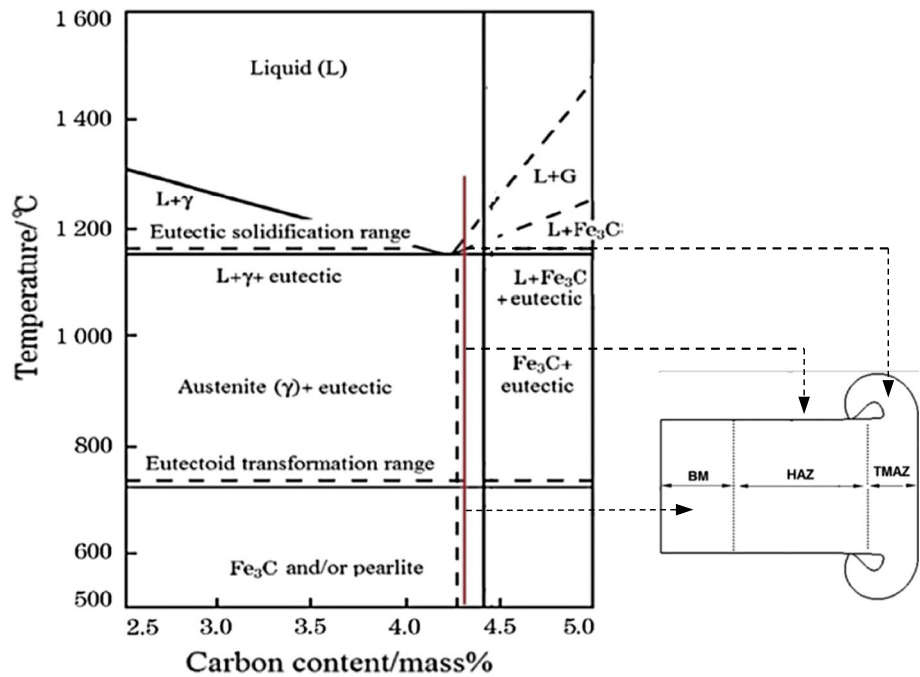
Fig. 7 Fracture appearances of nodular cast iron welded joints for different welding parameters

Fig. 8 Schematic Fe–C binary phase diagram of cast iron weld with calculated carbon equivalent (red line indicates the investigated material) (color figure online)

$$C_{eq} = w_c + 0.31 \cdot w_{si} + 0.33 \cdot w_p + 0.45 \cdot w_s - 0.028 \cdot w_{Mn}$$

During friction welding of nodular cast iron, metal is heated above the eutectoid transformation temperature A_1 (see Fig. 4a) and transforms into austenite. At the end of the forging phase, said metal cools down below the eutectoid temperature and austenite decomposes into ferrite, pearlite, bainite, or martensite, which are daughter products (see binary phase diagram Fig. 8) [33–35].

Microstructure observations of the welded joints given in the form of a function of distance from the weld interface are given in Fig. 9. A thin proeutectoid ferrite layer
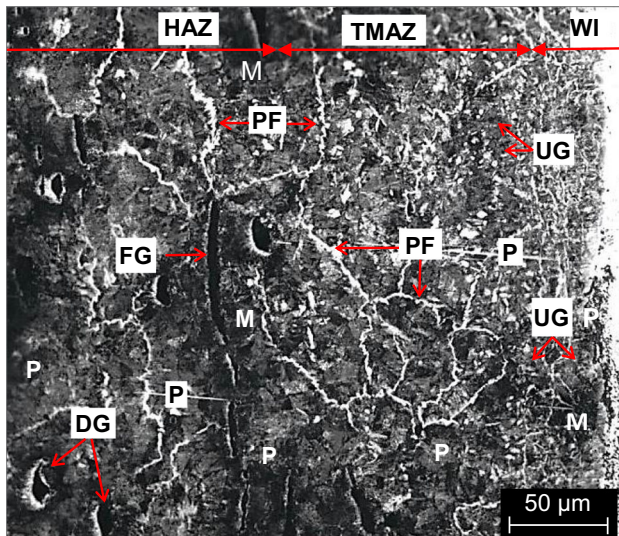
Fig. 9 Optical micrograph showing the microstructure of nodular cast iron friction-welded. *DG* deformed graphite, *FG* flake-shaped graphite, *M* martensite, *PF* proeutectoid ferrite, *UG* ultra-refined graphite. Magn. ×250

formed close to the weld interface in both central and peripheral zones (see Figs. 9, 10b). The peak temperature during welding reached 950 °C, thus in TMAZ, the process temperature was high enough to austenitize and coarsen the grains. Then the successive rapid cooling led to the facts that pearlite grains became coarse (Figs. 9, 10) and less ferrite precipitating at the pearlite grain boundary as reported in the papers [36, 37]. And this situation was more serious in TMAZ near the weld interface where the process temperature was higher, which suggested the microstructure was quite heterogeneous in this area [38]. Moreover, ferrite structures in the original ductile iron had transformed into acicular martensite structures (Figs. 9, 11a)

through rapid cooling from the high temperature state [34, 35]. When the temperature of nodular cast iron exceeds the temperature of eutectoid, carbon in graphite spreads out to speed up the microstructure transformation by increasing carbon concentration in the base metal. While rapidly cooling, austenite may transform into a martensite structure (Fig. 11) as demonstrated in other papers [39–43].

The identified microstructures of nodular cast iron in the HAZ included irregular and deformed graphite precipitates and a mixture of pearlite and ferrite. The proportion of pearlite was small in comparison to the one of ferrite. Ferrite was mainly present around the region of graphite nodules (Figs. 9, 12a). The outcomes of microscopic observations show that graphite morphology (size and shape) was changed in an increasing distance from the weld interface. In some areas of the micrograph, ultra-refined graphite particles (0.5–1 μm) were uniformly distributed in a pearlitic matrix (see Fig. 9). The spheroidal graphite morphology changed into almost flake-shaped graphites (Fig. 12) located along the weld interface, because of the heat and extensive mechanical deformation generated during the friction process [23, 24]. The length of flake-shaped graphite was approximately 50 μm (see Fig. 9). Using a high magnification, as given in Fig. 11b, numerous dense acicular martensite structures around the graphite nodules were distinctly presented. Martensite particles were approximately (2–6 μm) in size. Based on the phase transformation to martensite, the temperature of the HAZ during welding reached eutectoid temperature (see Fig. 8). Because the remaining time of eutectoid temperature was extremely short, only structures around graphite transformed into martensite while cooling as suggested by the authors of another paper [22].

Fig. 10 SEM micrograph of nodular cast iron welded joint showing **a** coarse pearlite with the deformed graphite Magn. ×5500 **b** proeutectoid ferrite network within the prior austenite grain boundaries at weld interface and TMAZ of the central zone. Magn. ×7500
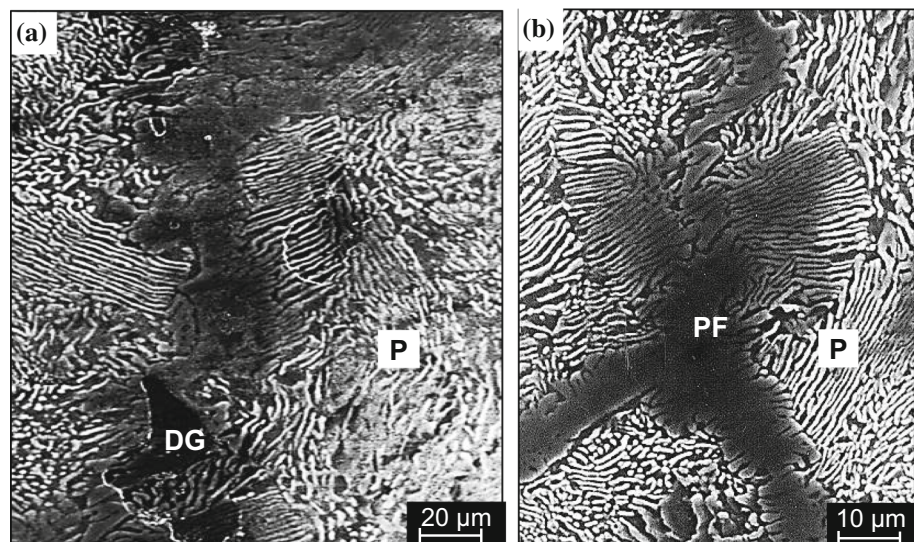
Fig. 11 SEM micrograph of nodular cast iron welded joint showing **a** acicular martensite. Magn. ×1000, **b** deformed graphite nodule embedded in the martensite structure at the weld interface and TMAZ of the central zone. Magn. ×500
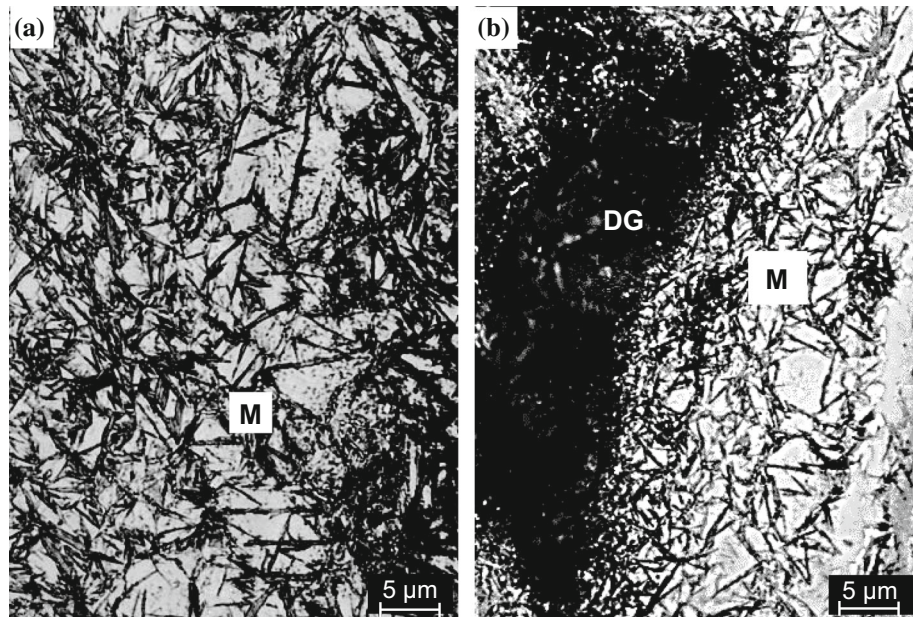
Fig. 12 SEM micrograph of nodular cast iron welded joint showing **a** flake-shaped graphite nodules embedded in a ferrite shell at TMAZ of the central zone. Magn. ×500, **b** formation of a stripe shaped graphite film at the weld interface of the central zone. Magn. ×500. *DG* deformed graphite, *LDSG* deformation layers of spheroidal graphite
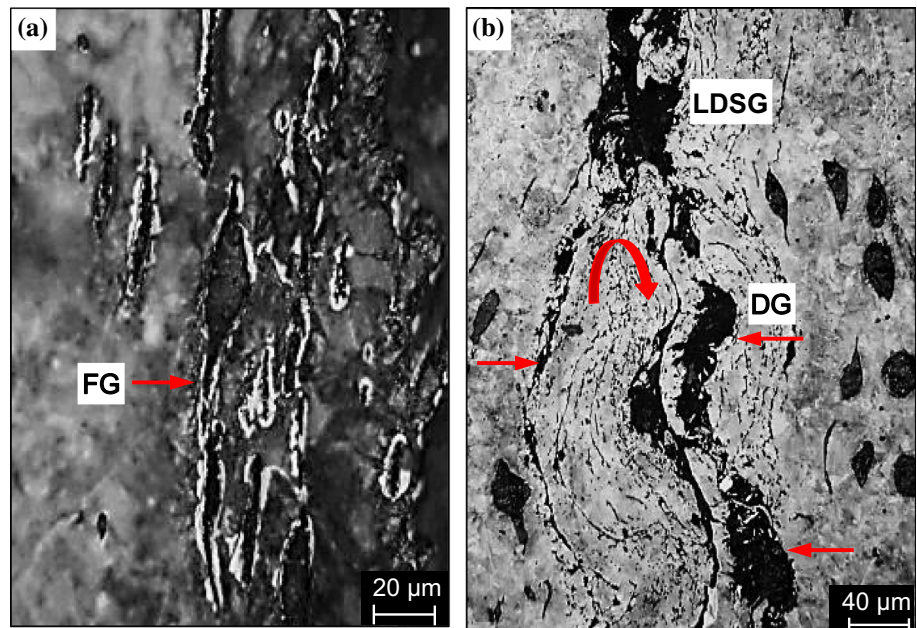
As it can be seen from Fig. 12, the process of friction welding is difficult, because graphite particles, distributed in metal matrix without ductility, deteriorate the deformation plastic flow in high temperature and act as a lubricant, not allowing for a sufficient frictional heat to process the material. Because the plastic deformation of spheroidal graphite during friction welding was significant, deformation layers of spheroidal graphite were observed (Fig. 12a). Authors [14] reported that an early softening of nodular cast iron and a constant transfer of graphite nodules to the joint plane, led to the formation of a new graphite film (see Fig. 12b). However, the appropriate welding conditions reduced the amount of deformation layers of spheroidal graphite in the joint of nodular cast iron, as demonstrated in another paper [18].

The increase in the amount of deformation in thickness (about 40%) led to the elongation of graphite through the metal matrix. It is clear that, at this high amount of reduction, the matrix was deformed around graphite, especially at both sharp ends of angular graphite. Consequently, in the vicinity of graphite clusters areas of striations were created. These striations passed through many grains without deviation, resulting in a severe localized micro-cracking. The micro-cracks were often observed

along matrix grain boundaries. Similar trend was reported in yet another paper [44].
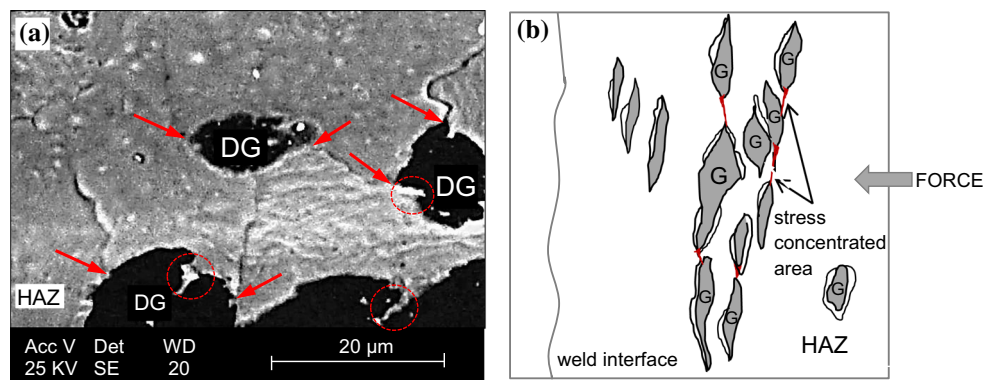
3.8 Cracking observation

Figure 13a shows the observed cracks. It can be seen that there are multiple cracks and deformed graphite nodules in the path of the cracks. The cracks are visible around the graphite and some cracks are actually in the graphite (circle in Fig. 13a). Extensive investigation of the situation when there was a lower crack severity showed that the graphite indeed deformed nodule particles were initiation sites for the cracks (arrows in Fig. 13a). However, when thermal stress was further developed in the adjacent areas, another crack initiated from the graphite particle and propagated in the metal matrix [44]. The connection of these minor cracks led to the formation of large major cracks, which run through martensite structures. Similar crack mechanism has been observed in case of powder welding process in other papers [45, 46].
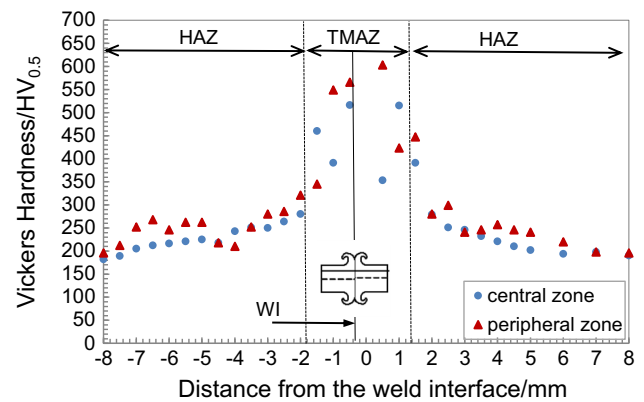
Figure 13b shows a schematic representation of cracking in the HAZ of a nodular cast iron in the case of friction welding process. As it can be seen, the marked areas are critical, because probably the highest stress can be identified there. The ellipsoidal or even flake-shaped graphite in the HAZ acts as a stress concentration, which may prematurely cause a localized plastic flow at low stress and initiate fracture in the matrix at higher stress (Fig. 13a). Moreover, graphite flakes deflect a passing crack and initiate countless new cracks as the material breaks. As a result, this graphite morphology exhibits no elastic behavior and fails in tension without a significant plastic deformation [13, 47].

3.9 Microhardness

Figure 14 shows the Vicker's hardness profile of the nodular cast iron cross-section following welding process.

Fig. 14 Vicker's hardness distributions of nodular cast iron friction-welded joint

The hardness of the TMAZ, HAZ, and parent material region was measured. The hardness value of the nodular cast iron parent material was approximately 185–195 HV. According to the microhardness curve of the peripheral zone, the maximal hardness value reached 605 HV in the TMAZ because numerous martensite structures were observed in this region (see Fig. 11a). Martensite was generated because the material was intensively heated and rapidly cooled down during the welding process [23, 24]. The high hardness of the peripheral zone suggests that the carbon content of the martensite structures was relatively high. The result shows that the hardness of the welded sample decreased more rapidly when the phase changed from a fully deformed zone to the HAZ. As can be observed in Fig. 14, hardness decreases much slower in the HAZ and extends to 7 mm from the weld interface. The hardness value of this region ranged between 210 and 310 HV, which remained higher than that of the parent material. The hardness value of the central zone was slightly lower than the one of the peripheral zone, and the hardness of the parent material was the lowest. The maximum hardness value of the central zone, indicated in the TMAZ,

Fig. 13 Cracks in nodular cast iron friction-welded joint **a** SEM image of the path of crack propagation at the HAZ of the central zone, **b** schematic stress concentrated area in nodular cast iron during friction welding. Magn. ×2000

was equal to 516 HV. As expected, hardness close to the weld zone was much higher than the hardness of the HAZ and the parent material (see Table 1). Variations of hardness in the welding interface were directly associated with the changes in the microstructure subjected to a high temperature and plastic deformation [3]. Earlier studies have indicated that when a carbon alloy is used in the welding process, refined grains are generated at the weld because of the dynamic recrystallization caused by a severe plastic deformation at high temperatures. After cooling and applying the subsequent pressure, the process of recrystallization and growth takes place that results in fine grain structure as demonstrated authors in the papers [33, 48]. Moreover, according to the Hall–Petch relation, this would result in higher strength of the welded joint as reported [49].The structure of these refined grains comprised a lot of dislocation phenomena as reported by authors [47, 50].

## 3.10 Effect of welding parameters on tensile strength of welded joints

A tensile test was applied after machining weld flashes formed during the friction welding process. The effect of friction time on the ultimate tensile strength (UTS) of welded joints and flash diameter can be seen in Fig. 15a, b. Friction time was changed from 30 to 240 s. In Fig. 15a it can be seen that the tensile strength of the joints increased together with increasing friction time for nodular cast iron samples. Increase in friction time leads to more amount of heat generation at the weld interfaces as reported in the papers [51, 52]. However, the results of tensile strength obtained for the welds were not satisfactory. The maximum tensile strength was increased up to the value of 234 MPa, which was 53% efficiency of nodular cast iron strength base material. In addition, it can be seen that the UTS increased quickly with increasing upsetting pressure.

The effect of friction time on flash diameter is presented in Fig. 15b. It can be seen that flash diameter increased together with increasing friction time. Similar results for the relationship between welding parameters, flash diameter, and tensile strength were achieved for different joints in other papers [25, 26].

The effect of friction time on axial shortening is presented in Fig. 15c. It is clearly seen that axial shortening increased together with increasing friction time. A similar trend was observed by authors [49, 53]. The combination of high friction welding parameters produced more axial shortening that played an important role in the mechanical properties of the joints, as reported by authors of other works [27, 28].

Fig. 15 Effect of welding parameters on ultimate tensile strength of nodular cast iron joints. The relationship between **a** friction time and ultimate tensile strength, **b** friction time and flash diameter, **c** friction time and axial shortening
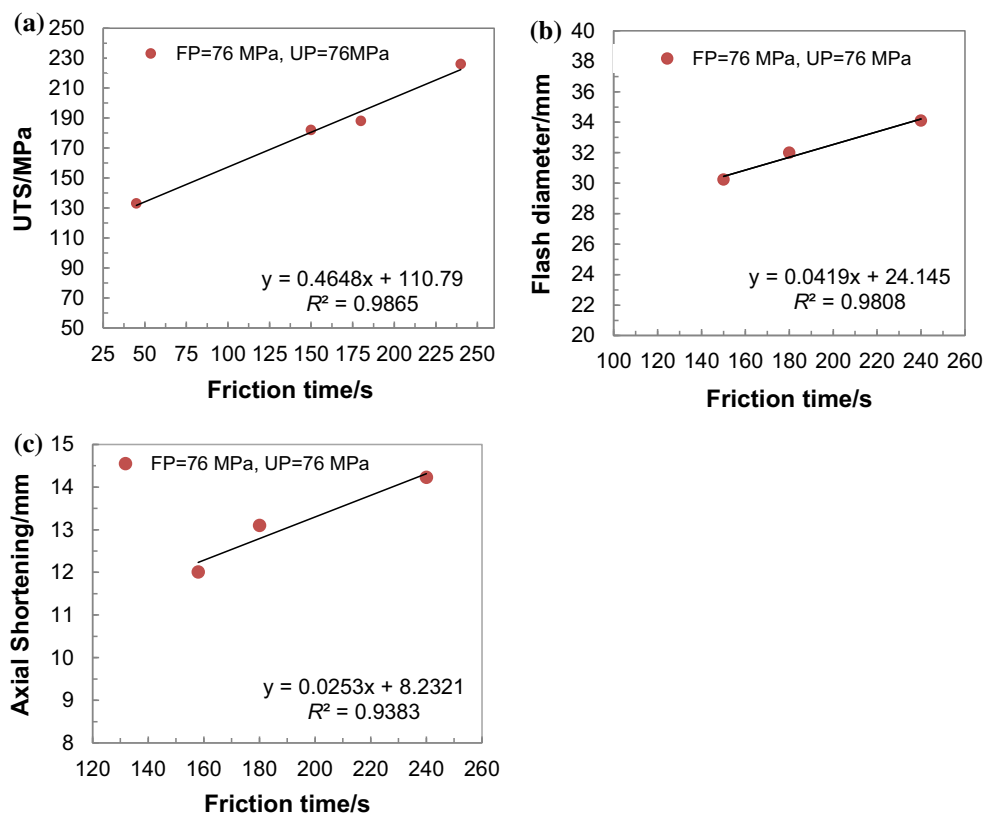
3.11 Fractography

The fracture surfaces of the tensile tested specimens were identified by means of scanning electron microscopy so as to understand failure patterns. The failure of the joints occurred only in the form of a fracture along the interface. Figure 16 shows a fracture surface micrograph of the tensile specimen fabricated using optimum parameters. It can be seen that two dissimilar fracture morphologies were distinguished in nodular cast iron welds. The fracture observation of the peripheral zone sample showed a cleavage fracture with river markings on the facets (Fig. 16a, b). River markings on the facets resulted from the propagation of the crack on a number of planes of different levels [46]. The cleavage planes of {100} or {110} type were clearly observed in the immediate vicinity of the graphite nodule. Additionally, martensite also cleaved along the {100} planes. Due to significant differences in orientations of single martensite blocks, crossing grain boundaries by a crack was hindered. In this case, the river pattern could be barely noticed (Fig. 16b). The cleavage planes are characteristic for ferrite, which forms a specific shell around graphite nodule [27]. In the case of brittle fracture, little to no visible plastic deformation precedes the fracture. Generally, a brittle fracture propagates through the grains. However, in the case of high-strength material, the crack follows grain boundaries [47].

The fracture observed in the central zone sample showed the ductile mode of the fracture surface (Fig. 16c). Cavities arose from inclusions or coarser precipitates were enlarged

and—during further yielding—the material between them was necked and sheared. Moreover, a microvoid coalescence (MVC) seems to be the dominant form of the fracture region (Fig. 16c). The dimple pattern around graphite nodules showed the deformation of the surrounding ferrite during the final period of straining up to fracture. Additionally, Fig. 16c, d demonstrates a relatively large cavity size, especially in comparison to the graphite nodule size. According to the authors of yet another publication, [29] the formation of these cavities may be attributed to decohesion of graphite and the surrounding matrix, as demonstrated in Fig. 15d.

4 Conclusions

The following conclusions can be drawn from this paper:

1. Friction welding of nodular cast iron can be successfully carried out without any interlayers and heat treatment. The maximum average strength of 226 MPa, which is 53% of the parent material, can be achieved for the friction time of 240 s and friction pressure of 76 MPa. Tensile strength increases with friction time and slightly decreases with increasing upset pressure under experimental conditions.
2. Maximum hardness value of the peripheral zone reached 605 HV because many martensite structures were observed in this region.
3. During friction welding of nodular cast iron, both high temperature (about 950 °C) and carbon content

Fig. 16 Fracture surface micrographs showing a mixture of dimple and a cleavage pattern mode for tensile test specimen with the optimum parameters **a**, **b** cleavage fracture with river markings; **c**, **d** shallow dimples with microvoid coalescence visible in the central part of the micrograph
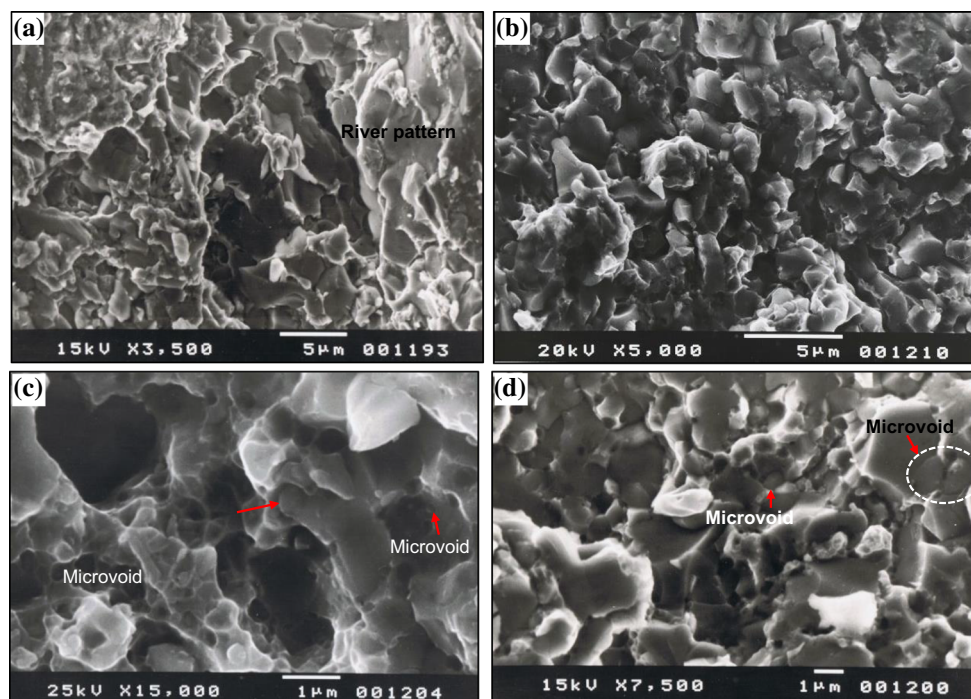
significantly affected microstructure transformation. Final microstructures in welding zones of friction weld were composed of pearlite, proeutectoid ferrite, and acicular martensite around the graphite nodules.

4. Graphite in the surface zone exhibited a striped configuration and distinct martensite structures formed in the metal matrix. Graphite in the central zone remained in the form of individual granules and acicular martensite was observed outside the graphite nodules.

5. Ellipsoidal or even flake-shaped graphite in the HAZ acts as a stress raiser, which may cause a localized plastic flow prematurely and initiate fracture in the metal matrix. Cracks occur mostly at the interface of deformed graphite nodules and then spread through grain boundaries of the metal matrix.

References

1. Davis JR (1996) ASM speciality handbook: cast irons. ASM International, Materials Park
2. Handbook ASM (1995) Properties and selection iron and steel. ASM International, Materials Park
3. Handbook Welding (1991) Welding process, 8th edn. AWS, Miami
4. Kou Sindo (2003) Welding metallurgy, 2nd edn. Wiley, Hoboken
5. Pascual M, Cembrero J, Salas F (2008) Analysis of the weldability of ductile iron. Mater Lett 62:1359–1362
6. Klimpel A (1998) The problem of welding cast irons is examined taking the example of a spheroidal cast iron. Weld Int 12:20–24
7. El-Banna EM (1999) Effect of preheat on welding of ductile cast iron. Mater Lett 41:20–26
8. Handbook ASM (1992) Metallography and microstructures. ASM International, Materials Park
9. Handbook Welding (2000) Metals and their weldability, 7th edn. AWS, Miami
10. Crossland B (1971) Friction welding. Contemp Phys 12:559–574
11. American Welding Society (1989) Specifications and standards. In: American Welding Society (ed) Recommended practice for friction welding. AWS, Miami
12. Lebedev VK, Chernenko IA (1992) Welding and surface reviews friction welding. Harwood Academic Publishers, Amsterdam
13. Handbook ASM (2002) Failure analysis and prevention. ASM international, Materials Park
14. Mitelea I, Craciunescu CM, Gugu R (2010) Interfacial behavior of dissimilar friction welded nodular cast irons with low carbon steels. Mater Sci Forum 638:3757–3762
15. Richter H, Palzkill A (1985) Applicability of test result from miniature friction welded specimens to full-size specimens as demonstrated by the combination of constructional steel and spheroidal graphite cast iron. Weld Cut 37:60–65
16. Dette M, Hirsch J (1990) Reibschweissen von Konstruieren aus Kugelgraphitguss mit Stahlteilen. Schw und Schn 11(42):188–190
17. Shakhmatov MV, Shakhmatov DM (2004) Features of resistance butt welding of cast iron. Weld Int 18(9):737–741
18. Michiura Y, Maekawa K, Takahara W, Kitagawa M, Horie H (1998) Friction welding of ductile cast iron pipes. Jpn J Foundry Eng Soc 70:873–877
19. Shinoda T, Endo S, Kato Y (1999) Friction welding of cast iron and stainless steels. Weld Int 13(2):89–95
20. Ochi H, Kawai G, Morikawa K, Yamamoto Y, Suga Y (2007) Macrostructure and temperature distribution near the weld interface in friction welding of cast iron. Strength Fract Complex 5:79–88
21. Chen Hai-Yan Fu, Li Zhang Wen-Yuan, Fen-Jun Liu (2015) Radial distribution characteristics of microstructure and mechanical properties of Ti–6Al–4V butt joint by rotary friction welding. Acta Metall Sin (Eng Lett) 28(10):1291–1298
22. Winiczenko R, Goroch O, Krzyńska A, Kaczorowski M (2017) Friction welding of tungsten heavy alloys with aluminium alloy. J Mater Process Technol 246:42–55
23. Cheng CP, Lin HM, Lin JC (2010) Friction stir welding of ductile iron and low carbon steel. Sci Technol Weld Join 15:706–711
24. Chang HT, Wang CJ, Cheng CP (2013) Friction stir lap welded low carbon steel and ductile iron: microstructure and mechanical properties. Sci Technol Weld Join 18(8):688–696
25. Chang HT, Wang CJ, Cheng CP (2014) Microstructure feature of friction stir butt-welded ferritic ductile iron. Mater Des 56:572–578
26. Winiczenko R, Kaczorowski M (2012) Friction welding of ductile cast iron using interlayers. Mater Des 34:444–451
27. Winiczenko R, Kaczorowski M (2013) Friction welding of ductile iron with stainless steel. J Mater Process Technol 213:453–462
28. Winiczenko R, Kaczorowski M (2016) Friction welding: ductile irons. In: Colás R, Totten GE (eds) Encyclopedia of iron, steel, and their alloys. CRC Francis & Taylor Group, New York, p 1149
29. Winiczenko R (2016) Effect of friction welding parameters on the tensile strength and microstructural properties of dissimilar AISI 1020-ASTM A536 joints. Int J Adv Manuf Technol 84:941–955
30. Winiczenko R, Sałat R, Awtoniuk M (2013) Estimation of tensile strength of ductile iron friction welded joints using hybrid intelligent methods. Trans Nonferr Met Soc China 3(2):385–391
31. Huang Y, Zhu Y (2008) Failure analysis of friction weld (FRW) in truck axle application. J Fail Anal Prevent 8(1):37–40
32. ASTM E8M–04 (2010) Standard test methods for tension testing of metallic materials. ASTM International, Materials Park
33. Rajesh Jesudoss Hynes N, Shenbaga Velu P, Nithin AM (2018) Friction push plug welding in airframe structures using Ti–6Al–4V plug. J Braz Soc Mech Sci Eng 40(158):1–7
34. Baker H (1990) Alloy phase diagram. In: ASM handbook, vol 3. Materials Park

35. Dieter GE (1986) Mechanical metallurgy. McGraw-Hill Co., New York
36. Ma H, Qin G, Geng P, Li F, Fu B, Meng X (2015) Microstructure characterization and properties of carbon steel to stainless steel dissimilar metal joint made by friction welding. Mater Des 86:587–597
37. Ma H, Qin G, Geng P, Li F, Meng X, Fu B (2016) Effect of post-weld heat treatment on friction welded joint of carbon steel to stainless steel. J Mater Process Technol 227:24–33
38. Nguyen TC, Weckman DC (2006) A thermal and microstructure evolution model of direct-drive friction welding of plain carbon steel. Metall Mater Trans B 37:275–292
39. Martines RA, Asikera JA (1995) Pearlitic nodular cast iron: can it be welded? Weld J 74:65–70
40. Voight RC, Loper CR (1983) Study of heat affected zone structures in ductile cast iron. Weld J 62:82–88
41. Nippes EF (1960) Heat affected zone of arc welded ductile iron. Weld J 39:465–476
42. Pease GR (1960) Welding of ductile iron. Weld J 39:1–9
43. El-Bitar T, El-Banna E (1997) Contribution of forming parameters on the properties of hot rolled ductile cast iron alloys. Mater Lett 31:145–150
44. Ebrahimnia M, Malek Ghainia F, Gholizadea Sh, Salarib M (2012) Effect of cooling rate and powder characteristics on the soundness of heat affected zone in powder welding of ductile cast iron. Mater Des 33:551–556
45. Malek Ghaini F, Ebrahimnia M, Gholizade Sh (2011) Characteristics of cracks in heat affected zone of ductile cast iron in powder welding process. Eng Fail Anal 18:47–51
46. Kaczorowski M, Winiczenko R (2013) The microstructure and mass transport during friction welding of ductile cast iron. Ind Lubr Tribol 65:251–258
47. Calvo FA, Urena A, Gomez de Salzar JM, Molleda F (1989) Diffusion bonding of grey cast iron to Armco iron and a carbon steel. J Mater Sci 24(11):4152–4159
48. Akbari Mousavi SAA, Rahbar Kelishami A (2008) Experimental and numerical analysis of the friction welding process for the 4340 steel and mild steel combinations. Weld J 87:178–186
49. Rajesh Jesudoss Hynes N, Nagaraj P, Angela Jennifa Sujana J (2014) Mechanical evaluation and microstructure of friction stud welded aluminium-mild steel joints. Arab J Sci Eng 39:5017–5023
50. Pineau A, Benzerga AA, Pardoen T (2016) Failure of metals I: brittle and ductile fracture. Acta Mater 107:424–483
51. Rajesh Jesudoss Hynes N, Shenbaga Velu P (2017) Simulation of friction welding of alumina and steel with aluminum interlayer. Int J Adv Manuf Technol 93:121–127
52. Rajesh Jesudoss Hynes N, Nagaraj P, Angela Jennifa Sujana J (2012) Investigation on joining of aluminium and mild steel by friction stud welding. Mater Manuf Process 27:1409–1413
53. Rajesh Jesudoss Hynes N, Nagaraj P, Palanichamy R, Arumugham CAK, Angela Jennifa Sujana J (2014) Numerical simulation of heat flow of friction stud welding of dissimilar metals. Arab J Sci Eng 39:3217–3224